Eur. Phys. J. B **51**, 571–581 (2006)
DOI: 10.1140/epjb/e2006-00252-4

THE EUROPEAN PHYSICAL JOURNAL B

Electronic instabilities in 3D arrays of small-diameter (3, 3) carbon nanotubes

J. González[1] and E. Perfetto[1,2,a]

[1] Instituto de Estructura de la Materia, Consejo Superior de Investigaciones Científicas, Serrano 123, 28006 Madrid, Spain
[2] Istituto Nazionale di Fisica Nucleare - Laboratori Nazionali di Frascati, via E. Fermi 40, 00044 Frascati, Italy

Received 21 October 2005
Published online 22 June 2006 –

Abstract. We investigate the electronic instabilities of the small-diameter (3, 3) carbon nanotubes by studying the low-energy perturbations of the normal Luttinger liquid regime. The bosonization approach is adopted to deal exactly with the interactions in the forward-scattering channels, while renormalization group methods are used to analyze the low-energy instabilities. In this respect, we take into account the competition between the effective e–e interaction mediated by phonons and the Coulomb interaction in backscattering and Umklapp channels. Moreover, we apply our analysis to relevant experimental conditions where the nanotubes are assembled into large three-dimensional arrays, which leads to an efficient screening of the Coulomb potential at small momentum-transfer. We find that the destabilization of the normal metallic behavior takes place through the onset of critical behavior in some of the two charge stiffnesses that characterize the Luttinger liquid state. From a physical point of view, this results in either a divergent compressibility or a vanishing renormalized velocity for current excitations at the point of the transition. We observe anyhow that this kind of critical behavior occurs without the development of any appreciable sign of superconducting correlations.

PACS. 71.10.Pm Fermions in reduced dimensions – 73.22.-f Electronic structure of nanoscale materials: clusters, nanoparticles, nanotubes, and nanocrystals – 73.63.Fg Nanotubes

1 Introduction

The development of nanoscale technology during the last decade has attracted much attention on carbon nanotubes, which are among the most promising candidates to fabricate molecular-size devices. This is mainly due to the wide variety of their electronic and transport properties, which can result in metallic [1], semiconducting [2] or even superconducting behavior [3], depending on geometry and the way of assembling.

From a theoretical point of view, the confinement of electrons in the longitudinal dimension of the nanotubes induces the so-called Luttinger liquid behavior [6–10]. This is characterized, for instance, by the power-law dependence of the differential conductance, which has been actually observed experimentally [4,5].

Such a behavior breaks down anyhow at sufficiently low temperature, and the nanotubes enter a different regime, usually driven by the quality of the contacts in the experimental setup. In particular, in the case of very transparent contacts, it has been observed that carbon nanotubes may develop superconducting correlations, inherited from superconducting electrodes (proximity effect) [3] as well as intrinsic to large assemblies of massive ropes [11,12].

The superconducting instability is anyway in competition with the so-called Peierls (or charge-density-wave) instability, which may induce a metallic-semiconducting transition caused by a lattice distortion. The mean-field temperature T_P of such a transition has been estimated by means of detailed calculations, and it is predicted to increase as the radius of the nanotubes becomes smaller [13]. For tubes of typical radius, calculations find a very low (undetectable) value of T_P, while for thinner nanotubes it is predicted to be significantly larger and competing with the superconducting critical temperature.

Nevertheless, superconductivity at about 15 K has been claimed to occur in 4 Å-diameter nanotubes [14]. In the experiment reported in reference [14], a strong diamagnetic behavior was interpreted as an anisotropic Meissner effect, while a genuine superconducting transition was not observed. This has opened some controversy on this issue, since ab initio simulations predict a room-temperature Peierls transition in the allowed 4 Å-diameter geometries, namely in the (5, 0) [15] and the (3, 3) nanotubes [16]. On the other hand, mean-field calculations for the (5, 0) nanotubes seem to find a superconducting instability, but with a critical temperature of about 1 K [17].

In this paper we investigate the low-energy properties of the (3, 3) nanotubes by focusing on the instabilities of the Luttinger liquid behavior. We study carefully the competition between the effective e–e interaction

[a] e-mail: enrico.perfetto@roma2.infn.it

mediated by phonons and the Coulomb repulsion. The bosonization technique is applied in order to deal exactly with the interactions in the forward-scattering channels, while renormalization group methods are used to approach the low-energy instabilities of the system, driven by the backscattering and Umklapp interactions. Moreover, we pay also special attention to the experimental conditions reported in reference [14], which lead to large arrays of nanotubes embedded in a zeolite matrix. This gives rise to a large screening of the Coulomb potential, which has no counterpart in the case of single nanotubes [18,19]. We study this effect by means of a generalized RPA approach, showing that the long-range intertube coupling produces an efficient screening of the intratube interactions with small momentum-transfer.

The most important result of the present study is the finding of two different low-energy phases characterized by critical (nonanalytic) behavior of the physical observables. Under the conditions corresponding to the experimental samples described in reference [14], the critical behavior is related to the vanishing of one of the Luttinger liquid parameters, and it is qualitatively consistent with the large diamagnetic signal observed in reference [14]. We also observe that this kind of singularity occurs well before the development of any sizeable superconducting or charge-density-wave correlations in the electron system.

2 Luttinger liquid approach to forward-scattering interactions

We start by paying attention to the interactions mediated by the Coulomb potential, which provides a strong source of repulsion between electrons in single nanotubes. In the tubular nanotube geometry, the Coulomb potential is given by [7]

$$V_C(\mathbf{r}-\mathbf{r}') = \frac{e^2/\kappa}{\sqrt{(x-x')^2 + 4R^2\sin^2[(y-y')/2R] + a_z^2}} \tag{1}$$

where the x coordinate goes along the longitudinal direction and y is the coordinate around the waist of the nanotube. R is the nanotube radius and the parameter $a_z \simeq 1.6$ Å is dictated by the size of the π carbon orbitals [7]. The screening by the environment of external charges is in general encoded in the dielectric constant κ. For the sake of studying the nanotube transport properties, it is more convenient do deal with the one-dimensional (1D) projection of the potential onto the longitudinal dimension of the nanotube. This is achieved by integration of the circular coordinate, upon which we obtain the 1D Coulomb potential $\tilde{V}_C(k)$ depending on the longitudinal momentum-transfer k [20]

$$\tilde{V}_C(k) \approx \frac{2e^2}{\kappa}\log\left(\frac{k_c+k}{k}\right), \tag{2}$$

k_c is in general of the order of the inverse of the nanotube radius R, as it is the memory that the 1D projection keeps of the finite transverse size.

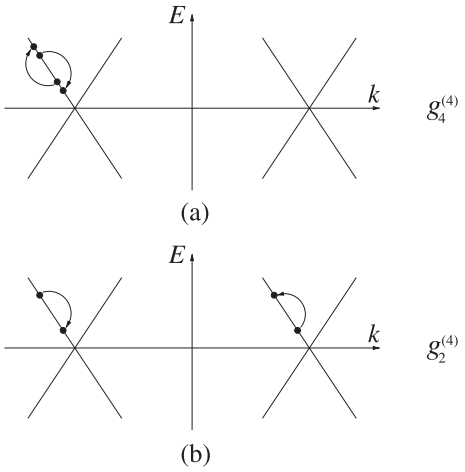

Fig. 1. Small momentum-transfer processes corresponding to the couplings $g_4^{(4)}$ and $g_2^{(4)}$.

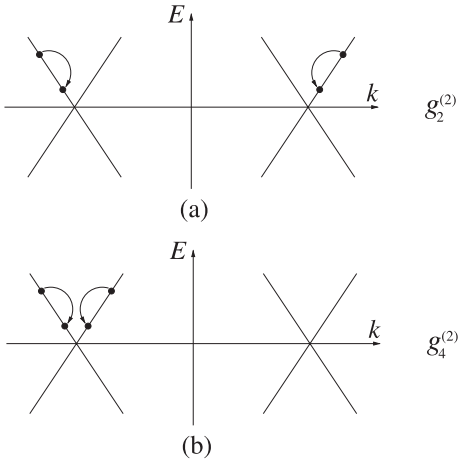

Fig. 2. Small momentum-transfer processes corresponding to the couplings $g_2^{(2)}$ and $g_4^{(2)}$.

The relative strength of the Coulomb interaction is given by the dimensionless ratio between e^2 and the Fermi velocity v_F, which can be evaluated from the constant $e^2/c \approx 1/137$ and the estimated Fermi velocity for the (3, 3) nanotubes [21]. This turns out to be $v_F \approx 7.5 \times 10^5$ m s^{-1}, which leads to a ratio $e^2/v_F \approx 2.9$. This means that the Coloumb potential should give the dominant interaction in the forward-scattering channels, at least in single nanotubes. The processes can be classified depending on the low-energy linear branches involved in the electron-electron scattering [22]. We recall at this point that the low-energy modes of the (3, 3) nanotubes lie in a bonding and an antibonding subband that cross at two Fermi points (in the undoped system) with opposite longitudinal momenta [21]. We can distinguish in particular four forward-scattering channels, labelled by their respective couplings as represented in Figures 1 and 2. In these processes there is a nominally strong Coulomb repulsion between the electrons, as they scatter without change of their chirality and the interaction strength is simply given by the Coulomb potential (2).

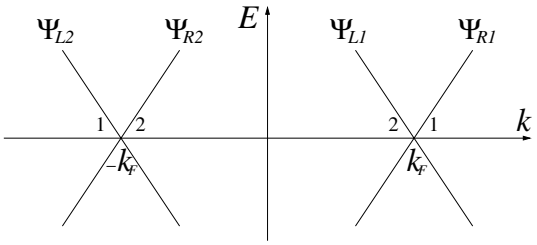

Fig. 3. Schematic representation of the low-energy branches arising from the bonding and the antibonding subband of the armchair nanotubes.

The interaction channels represented in Figures 1 and 2 are only part of the complete catalogue of scattering processes, that may be classified according to the chiralities and momentum-transfer for the interacting electrons [22]. It has become usual to assign respective coupling constants $g_i^{(j)}$ to the interaction channels, in such a way that the lower index discerns whether the interacting particles shift from one Fermi point to the other ($i = 1$), remain at different Fermi points ($i = 2$), or they interact near the same Fermi point ($i = 4$). The upper label follows the same rule to classify the different combinations of left-movers and right-movers, including the possibility of having Umklapp processes ($j = 3$). As we will see, the couplings for the channels with large momentum-transfer $2k_F$ or change of chirality of the interacting electrons have an strength which is sensibly smaller than that of the forward-scattering couplings represented in Figures 1 and 2.

A very important point is that the system with just the forward-scattering interactions $g_4^{(4)}, g_2^{(4)}, g_2^{(2)}$ and $g_4^{(2)}$ is exactly solvable by means of bosonization techniques [23–25]. Thus, no matter that the Coulomb repulsion may place these interaction channels in the strong-coupling regime, the availability of an exact solution makes possible to capture the nonperturbative effects coming from the Coulomb interaction. The bosonization techniques make use of the fact that the forward-scattering interactions can be written in terms of the electron density operators corresponding to the different electron fields $\Psi_{ri\sigma}$ for the linear branches shown in Figure 3. We adopt a notation in which the index $r = L, R$ is used to label the left- or right-moving character of the linear branch, and the index $i = 1, 2$ to label the Fermi point. The index σ stands for the two different spin projections. We may actually introduce the charge and spin density operators

$$\rho_{ri}(x) = \frac{1}{\sqrt{2}}\left(\Psi^\dagger_{ri\uparrow}(x)\Psi_{ri\uparrow}(x) + \Psi^\dagger_{ri\downarrow}(x)\Psi_{ri\downarrow}(x)\right) \quad (3)$$

$$\sigma_{ri}(x) = \frac{1}{\sqrt{2}}\left(\Psi^\dagger_{ri\uparrow}(x)\Psi_{ri\uparrow}(x) - \Psi^\dagger_{ri\downarrow}(x)\Psi_{ri\downarrow}(x)\right). \quad (4)$$

As long as the Coulomb interaction and the interaction mediated by exchange of phonons do not depend on the spin of the interacting electrons, we will carry out the subsequent discussion in terms of the charge density operators $\rho_{ri}(x)$.

It is convenient, for instance, to introduce operators for the sum and the difference of charge densities in the bonding and the antibonding subbands of the armchair nanotubes:

$$\rho_{R\pm}(k) = \frac{1}{\sqrt{2}}(\rho_{R1}(k) \pm \rho_{R2}(k)) \quad (5)$$

$$\rho_{L\pm}(k) = \frac{1}{\sqrt{2}}(\rho_{L2}(k) \pm \rho_{L1}(k)). \quad (6)$$

In terms of these operators, the Hamiltonian for the forward-scattering interactions can be written in the form

$$\begin{aligned} H_{FS} = \frac{1}{2}v_F \int_{-k_c}^{k_c} dk \sum_{r=L,R}\sum_{i=\pm} \rho_{ri}(k)\rho_{ri}(-k) \\ +\frac{1}{2}\int_{-k_c}^{k_c}\frac{dk}{2\pi}\, 2\left(\rho_{R+}(k)\ \left(g_4^{(4)} + g_2^{(4)}\right)\ \rho_{R+}(-k)\right. \\ +\rho_{L+}(k)\ \left(g_4^{(4)} + g_2^{(4)}\right)\ \rho_{L+}(-k) \\ +\rho_{R-}(k)\ \left(g_4^{(4)} - g_2^{(4)}\right)\ \rho_{R-}(-k) \\ +\rho_{L-}(k)\ \left(g_4^{(4)} - g_2^{(4)}\right)\ \rho_{L-}(-k) \\ +2\rho_{R+}(k)\ \left(g_2^{(2)} + g_4^{(2)}\right)\ \rho_{L+}(-k) \\ \left.+2\rho_{R-}(k)\ \left(g_2^{(2)} - g_4^{(2)}\right)\ \rho_{L-}(-k)\right). \end{aligned} \quad (7)$$

where k_c stands again for the momentum cutoff dictated by the transverse size of the nanotube.

We observe that the symmetric and the antisymmetric combination of the charge operators in the two low-energy subbands decouple in the Hamiltonian (7). This can be completely diagonalized by first introducing boson fields $\Phi_+(x)$ and $\Phi_-(x)$ (and their respective conjugate momenta, $\Pi_+(x)$ and $\Pi_-(x)$) defined by

$$\partial_x\Phi_+(x) = \sqrt{\pi}(\rho_{L+}(x) + \rho_{R+}(x)) \quad (8)$$

$$\partial_x\Phi_-(x) = \sqrt{\pi}(\rho_{L-}(x) + \rho_{R-}(x)). \quad (9)$$

The Hamiltonian can be rewritten then in the form

$$\begin{aligned} H_{FS} = \frac{1}{2}u_+ \int dx \left(K_+(\Pi_+(x))^2 + \frac{1}{K_+}(\partial_x\Phi_+(x))^2\right) \\ +\frac{1}{2}u_- \int dx \left(K_-(\Pi_-(x))^2 + \frac{1}{K_-}(\partial_x\Phi_-(x))^2\right) \end{aligned} \quad (10)$$

with renormalized velocities u_+, u_- and charge stiffnesses K_+, K_- given by the expressions

$$u_\pm K_\pm = v_F + \frac{1}{\pi}\left(g_4^{(4)} \pm g_2^{(4)} - \left(g_2^{(2)} \pm g_4^{(2)}\right)\right) \quad (11)$$

$$u_\pm/K_\pm = v_F + \frac{1}{\pi}\left(g_4^{(4)} \pm g_2^{(4)} + \left(g_2^{(2)} \pm g_4^{(2)}\right)\right). \quad (12)$$

Upon application of the canonical transformation

$$\Phi_+ = \sqrt{K_+}\tilde{\Phi}_+\ ,\ \Pi_+ = \frac{1}{\sqrt{K_+}}\tilde{\Pi}_+ \quad (13)$$

$$\Phi_- = \sqrt{K_-}\tilde{\Phi}_-\ ,\ \Pi_- = \frac{1}{\sqrt{K_-}}\tilde{\Pi}_- \quad (14)$$

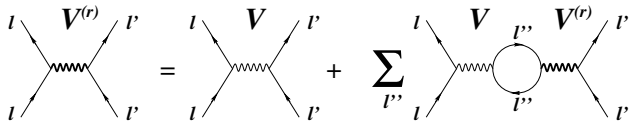

Fig. 4. Self-consistent diagrammatic equation representing the screening of the Coulomb potential between charges at nanotubes $\mathbf{l}$ and $\mathbf{l}'$. The sum over $\mathbf{l}''$ accounts for the polarization effects from all the nanotubes in the array.

the Hamiltonian (10) becomes that of a couple of noninteracting boson fields. This picture, in which the low-energy excitations are just given by charge fluctuations (and spin fluctuations with unrenormalized velocity), is what characterizes the Luttinger liquid regime of the electron system [23,24]. The charge stiffnesses and the renormalized velocities in the two different charge sectors dictate for instance the thermodynamic and transport properties, encoded into the compressibilities $\kappa_\pm$, the Drude weights $D_\pm$ and the dependence of the specific heat C_v on the temperature T [26]:

$$\kappa_\pm = \frac{2}{\pi}\frac{K_\pm}{u_\pm} \tag{15}$$

$$D_\pm = 2u_\pm K_\pm \tag{16}$$

$$\frac{C_v}{T} = \frac{\pi}{3}\left(\frac{1}{u_+}+\frac{1}{u_-}\right). \tag{17}$$

The above picture will be complemented later by including the effect of the backscattering and Umklapp interactions, that tend to destabilize the Luttinger liquid regime at low temperatures. At this point, we stress that the robustness of such a regime depends on the strength of the Coulomb interaction. The consideration of the screening effects induced by the environment becomes then quite relevant, specially in the case of a large assembly of nanotubes [18,19]. For the nanotube array described in reference [14], the long-range Coulomb repulsion gives rise to a nonnegligible interaction between electronic currents in different nanotubes. If we label these by their respective positions $\mathbf{l}$ and $\mathbf{l}'$ in the transverse section of the array, the intertube Coulomb potential can be expressed as

$$V_{\mathbf{l},\mathbf{l}'}(k) \approx \frac{2e^2}{\kappa} K_0(|\mathbf{l}-\mathbf{l}'|k), \tag{18}$$

where k denotes the longitudinal momentum-transfer. We recall that the Bessel function $K_0(x)$ is logarithmically divergent in the limit $x \to 0$. For $\mathbf{l} = \mathbf{l}'$, there is implicit a short-distance cutoff given by the radius of the nanotube, which leads then to the potential (2). The important point is that the intertube Coulomb potential gives rise to quite significant screening effects at small momentum-transfer, which modify appreciably the strength of the forward-scattering couplings described above.

In order to take into account the interaction among all the nanotubes in the array, we can adopt a generalization of the RPA scheme used in reference [27] for the study of 2D layered systems. In our case, the screened Coulomb potential $V^{(r)}_{\mathbf{l},\mathbf{l}'}(k)$ has to satisfy the self-consistent diagrammatic equation shown in Figure 4, with $\mathbf{l}''$ running over all the positions of the nanotubes in the array. We have then

$$V^{(r)}_{\mathbf{l},\mathbf{l}'}(k) = V_{\mathbf{l},\mathbf{l}'}(k) + \Pi \sum_{\mathbf{l}''} V_{\mathbf{l},\mathbf{l}''}(k)\, V^{(r)}_{\mathbf{l}'',\mathbf{l}'}(k), \tag{19}$$

where Π stands for the polarization of each 1D electron system. This function is known exactly at small momentum-transfer [24], and here it appears multiplied by the number of subbands $n = 2$ contributing at low-energies:

$$\Pi(k,\omega) = 2n\frac{1}{\pi}\frac{v_F k^2}{\omega^2 - v_F^2 k^2}. \tag{20}$$

Equation (19) can be easily solved by introducing the Fourier transform of the Coulomb potential with respect to the nanotube position $\mathbf{l}$ in the 2D transverse section of the array. We define for instance $\phi(\mathbf{p},k)$ by

$$V_{\mathbf{l},\mathbf{l}'}(k) = \left(\frac{d}{2\pi}\right)^2 \int_{BZ} d^2\mathbf{p}\, \phi(\mathbf{p},k)\, e^{i\mathbf{p}\cdot(\mathbf{l}-\mathbf{l}')}, \tag{21}$$

where d stands for the nanotube separation and BZ denotes that the integration is over the Brillouin zone for the nanotube lattice in the transverse section of the array. We define similarly $\phi^{(r)}(\mathbf{p},k)$ as the Fourier transform of $V^{(r)}_{\mathbf{l},\mathbf{l}'}(k)$. The expression of equation (19) becomes then in momentum space

$$\phi^{(r)}(\mathbf{p},k) = \phi(\mathbf{p},k) + \Pi\, \phi(\mathbf{p},k)\, \phi^{(r)}(\mathbf{p},k). \tag{22}$$

In what follows, we will stick to the solution of this equation at $\omega = 0$, for the sake of giving a simpler description of the screening effects in the static limit.

Within our RPA scheme, the screened Coulomb potential becomes finally

$$V^{(r)}_{\mathbf{l},\mathbf{l}'}(k) = \left(\frac{d}{2\pi}\right)^2 \int_{BZ} d^2\mathbf{p} \frac{\phi(\mathbf{p},k)}{1+2n\phi(\mathbf{p},k)/\pi v_F} e^{i\mathbf{p}\cdot(\mathbf{l}-\mathbf{l}')}. \tag{23}$$

The most important property of $V^{(r)}_{\mathbf{l},\mathbf{l}'}(k)$ is that it saturates at a finite value in the limit $k \to 0$. This is a reflection of the fact that, for distances much larger than the nanotube separation, the array screens effectively the Coulomb interaction as a 3D system. Thus, taking a value of the bare coupling $e^2 \approx 2.9 v_F$, we find that the intratube potential at vanishing momentum-transfer is $V^{(r)}_{\mathbf{l},\mathbf{l}}(k=0) \approx 0.75 v_F$ (for $\kappa = 1$). This value depends slightly on the dielectric constant, as represented in Figure 5. We will take this strength of the screened intratube Coulomb potential at $k = 0$ as an input for the values of the forward-scattering couplings $g_4^{(4)}, g_2^{(4)}, g_2^{(2)}$ and $g_4^{(2)}$ within each nanotube in the array.

A closer look at the above analysis shows that the Coulomb potential between nearest-neighbor nanotubes also gives rise to relevant interaction channels. The new couplings needed for a consistent description of the interaction processes are catalogued in Figure 7. They adhere to the same rules used to label the intratube couplings,

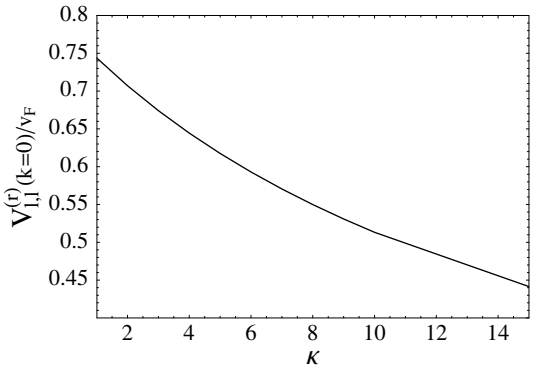

Fig. 5. Dependence of the screened intratube Coulomb potential (in units of v_F) on the dielectric constant κ.

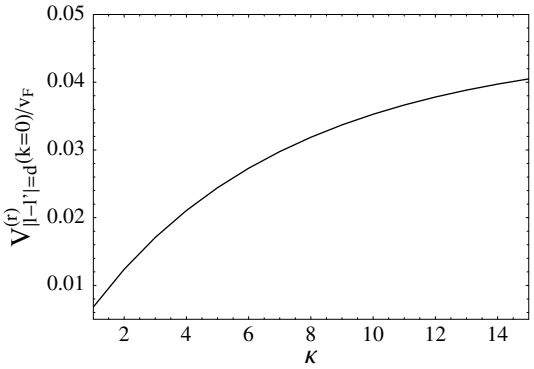

Fig. 6. Dependence of the screened intertube Coulomb potential (in units of v_F) on the dielectric constant κ.

but with a tilde to distinguish their intertube character. In particular, the intertube forward-scattering interactions $\tilde{g}_2^{(2)}$ and $\tilde{g}_4^{(2)}$ (preserving the chirality of the electrons within each nanotube) are affected by the screening effects described above, as they are corrected by the polarization of the different nanotubes in the array. Their strength is given by the intertube Coulomb potential, which keeps only a nonnegligible value between nearest-neighbor tubes, after screening by the nanotube array. Taking again $e^2 \approx 2.9 v_F$, the intertube potential for $|\mathbf{l} - \mathbf{l}'| = d$ has a value at vanishing momentum-transfer $V^{(r)}_{\mathbf{l},\mathbf{l}'}(k=0) \approx 0.007 v_F$ (for $\kappa = 1$). The dependence of this strength on the dielectric constant is shown in Figure 6. Although the relative strength of the intertube forward-scattering couplings $\tilde{g}_2^{(2)}$ and $\tilde{g}_4^{(2)}$ may appear small, these are however significant as they influence the scaling of the rest of interactions at low energies, as we will see in what follows.

3 Renormalization group scaling of the interactions

On the other hand, the intertube chirality-breaking interactions $\tilde{g}_2^{(1)}, \tilde{g}_4^{(1)}, \tilde{g}_2^{(3)}$ and $\tilde{g}_4^{(3)}$ give rise to a different kind of screening processes, of the type represented in Figure 8. The effect of these processes cannot be captured in the

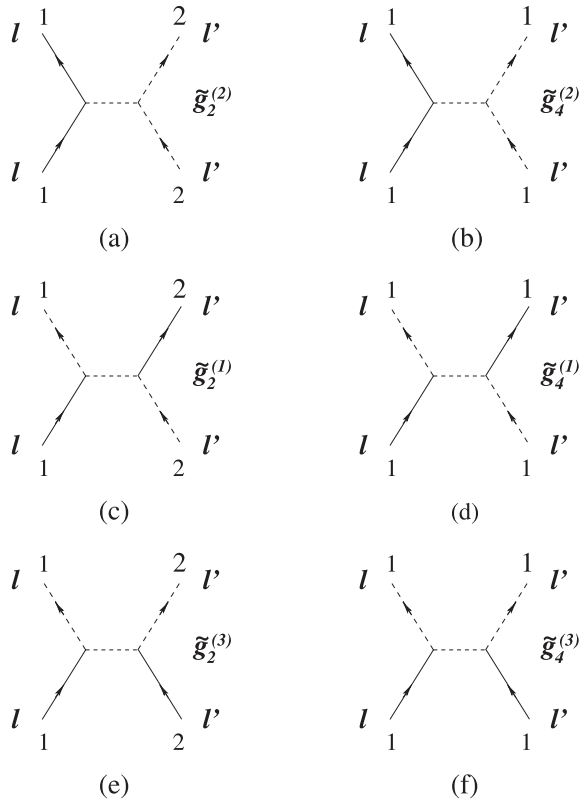

Fig. 7. Intertube interactions arising from the coupling between electronic currents in nearest-neighbor nanotubes $\mathbf{l}$ and $\mathbf{l}'$ of a 3D array. The full (dashed) lines represent the propagation of electrons with right (left) chirality, and the labels 1, 2 denote the respective Fermi points. The dashed lines (without arrow) stand for the intertube Coulomb potential.

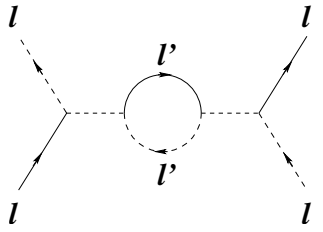

Fig. 8. Second-order process renormalizing backscattering interactions at a given nanotube $\mathbf{l}$ through the coupling with the nearest-neighbors $\mathbf{l}'$ in a 3D array of nanotubes. The dashed lines (without arrow) stand for the intertube Coulomb potential.

RPA scheme described above, as the polarization with a change of chirality in the particle-hole pair diverges logarithmically at low energies. As long as the corrections depend on the 1D cutoff, they give rise instead to new screening contributions to the scaling equations for the rest of interactions. We recall that the scaling equations for the interactions of single armchair nanotubes have been obtained in reference [22] (up to terms quadratic in the couplings). We have found that, after incorporating the corrections from the intertube interactions, the scaling

equations for the intratube couplings become

$$\frac{\partial g_1^{(1)}}{\partial l} = -\frac{1}{\pi v_F}\left(g_1^{(1)}g_1^{(1)} + g_1^{(2)}g_2^{(1)} + g_1^{(3)}g_1^{(3)} - g_1^{(3)}g_2^{(3)}\right) \quad (24)$$

$$\frac{\partial g_1^{(2)}}{\partial l} = \left(1 - \frac{1}{K_-}\right) g_1^{(2)} - \frac{1}{\pi v_F}\left(g_2^{(1)}g_1^{(1)} - g_4^{(3)}g_1^{(3)}\right) \quad (25)$$

$$\frac{\partial g_1^{(3)}}{\partial l} = (1-K_+)g_1^{(3)} - \frac{1}{\pi v_F}(2g_1^{(3)}g_1^{(1)} - g_2^{(3)}g_1^{(1)} - g_4^{(3)}g_1^{(2)}) \quad (26)$$

$$\frac{\partial g_2^{(1)}}{\partial l} = \left(1 - \frac{1}{K_-}\right) g_2^{(1)} - \frac{1}{\pi v_F}\left(2g_4^{(1)}g_2^{(1)} - g_4^{(1)}g_1^{(2)} + g_1^{(2)}g_1^{(1)} + g_4^{(3)}g_2^{(3)} - g_4^{(3)}g_1^{(3)} + 12\tilde{g}_4^{(1)}\tilde{g}_2^{(1)} + 12\tilde{g}_4^{(3)}\tilde{g}_2^{(3)}\right) \quad (27)$$

$$\frac{\partial g_2^{(2)}}{\partial l} = -\frac{1}{2\pi v_F}\left(g_2^{(1)}g_2^{(1)} + g_1^{(1)}g_1^{(1)} + g_1^{(2)}g_1^{(2)} - g_2^{(3)}g_2^{(3)}\right) \quad (28)$$

$$\frac{\partial g_2^{(3)}}{\partial l} = (1-K_+)g_2^{(3)} - \frac{1}{\pi v_F}\left(2g_4^{(1)}g_2^{(3)} + g_4^{(3)}g_2^{(1)} - g_4^{(3)}g_1^{(2)} - g_4^{(1)}g_1^{(3)} + 12\tilde{g}_4^{(1)}\tilde{g}_2^{(3)} + 12\tilde{g}_4^{(3)}\tilde{g}_2^{(1)}\right) \quad (29)$$

$$\frac{\partial g_4^{(1)}}{\partial l} = -\frac{1}{\pi v_F}\left(g_4^{(1)}g_4^{(1)} + g_2^{(1)}g_2^{(1)} - g_1^{(2)}g_2^{(1)} + g_2^{(3)}g_2^{(3)} - g_2^{(3)}g_1^{(3)} + 6\tilde{g}_4^{(1)}\tilde{g}_4^{(1)} + 6\tilde{g}_2^{(1)}\tilde{g}_2^{(1)} + 6\tilde{g}_4^{(3)}\tilde{g}_4^{(3)} + 6\tilde{g}_2^{(3)}\tilde{g}_2^{(3)}\right) \quad (30)$$

$$\frac{\partial g_4^{(2)}}{\partial l} = -\frac{1}{2\pi v_F}\left(g_4^{(1)}g_4^{(1)} - g_1^{(2)}g_1^{(2)} - g_1^{(3)}g_1^{(3)} - g_4^{(3)}g_4^{(3)}\right) \quad (31)$$

$$\frac{\partial g_4^{(3)}}{\partial l} = \left(2 - K_+ - \frac{1}{K_-}\right) g_4^{(3)} - \frac{1}{\pi v_F}\left(g_4^{(3)}g_4^{(1)} + 2g_2^{(3)}g_2^{(1)} - g_1^{(3)}g_2^{(1)} - g_2^{(3)}g_1^{(2)} - g_1^{(3)}g_1^{(2)} + 12\tilde{g}_4^{(1)}\tilde{g}_4^{(3)} + 12\tilde{g}_2^{(1)}\tilde{g}_2^{(3)}\right). \quad (32)$$

The variable l stands for minus the logarithm of the energy (temperature) scale measured in units of the high-energy cutoff of the 1D model $E_c \sim v_F k_c$ (of the order of $\sim$0.1 eV). The large coefficients in front of the intertube contributions arise from the number of nearest-neighbors of each nanotube in the 3D array. Furthermore, we have also incorporated a nonperturbative improvement of the equations by writing the exact dependence of the scaling dimensions on the forward-scattering couplings, expressed in terms of the K_+, K_- parameters. This is very convenient in order to investigate the instabilities that may appear when some of the forward-scattering couplings leave the weak-coupling regime. As we will see later, K_+ and $1/K_-$ may vanish as the scaling flow given by the l variable progresses towards low energies. The use of the nonperturbative scaling dimensions allows then to discern that the perturbative expansion in the forward-scattering couplings does not blow up away from the weak-coupling regime, and that instead it converges to well-behaved expressions in the scaling equations.

The new intertube interactions are themselves corrected by processes that diverge logarithmically at low energy, and that give rise to respective contributions to the scaling of the intertube couplings. We can focus on the analysis of $\tilde{g}_2^{(1)}, \tilde{g}_4^{(1)}, \tilde{g}_2^{(3)}$ and $\tilde{g}_4^{(3)}$, which have values given by the intertube potential (18) at the initial stage of the low-energy scaling. As long as this potential decays exponentially for $|\mathbf{l}-\mathbf{l}'|k > 1$, we can neglect the influence of other intertube interactions with $2k_F$ momentum-transfer. The second-order diagrams that renormalize the above intertube couplings consist of particle-particle processes or particle-hole loops involving a change of chirality, as illustrated in Figures 9 and 10. Some of the contributions depend on $\tilde{g}_2^{(2)}$ and $\tilde{g}_4^{(2)}$. This means that these couplings have to be taken into account for a consistent description of the low-energy scaling. The complete set of scaling equations for the intertube couplings becomes:

$$\frac{\partial \tilde{g}_2^{(1)}}{\partial l} = -\frac{1}{\pi v_F}\left(2g_4^{(1)}\tilde{g}_2^{(1)} + 2g_2^{(1)}\tilde{g}_4^{(1)} + 4\tilde{g}_4^{(1)}\tilde{g}_2^{(1)} + \tilde{g}_2^{(2)}\tilde{g}_2^{(1)} - g_4^{(2)}\tilde{g}_2^{(1)} - g_1^{(2)}\tilde{g}_4^{(1)} + 2g_2^{(3)}\tilde{g}_4^{(3)} + g_4^{(3)}\tilde{g}_2^{(3)} + 4\tilde{g}_2^{(3)}\tilde{g}_4^{(3)} - g_1^{(3)}\tilde{g}_4^{(3)}\right) \quad (33)$$

$$\frac{\partial \tilde{g}_2^{(3)}}{\partial l} = -\frac{1}{\pi v_F}\left(2g_4^{(1)}\tilde{g}_2^{(3)} + 2g_2^{(3)}\tilde{g}_4^{(1)} + 4\tilde{g}_4^{(1)}\tilde{g}_2^{(3)} + g_4^{(3)}\tilde{g}_2^{(1)} + 2g_2^{(1)}\tilde{g}_4^{(3)} + 4\tilde{g}_2^{(1)}\tilde{g}_4^{(3)} - g_1^{(3)}\tilde{g}_4^{(1)} - g_4^{(2)}\tilde{g}_2^{(3)} - g_1^{(2)}\tilde{g}_4^{(3)} - \tilde{g}_2^{(2)}\tilde{g}_2^{(3)}\right) \quad (34)$$

$$\frac{\partial \tilde{g}_4^{(1)}}{\partial l} = -\frac{1}{\pi v_F}\left(2g_4^{(1)}\tilde{g}_4^{(1)} + 2g_2^{(1)}\tilde{g}_2^{(1)} + 2\tilde{g}_4^{(1)}\tilde{g}_4^{(1)} + 2\tilde{g}_2^{(1)}\tilde{g}_2^{(1)} + \tilde{g}_4^{(2)}\tilde{g}_4^{(1)} - g_4^{(2)}\tilde{g}_4^{(1)} - g_1^{(2)}\tilde{g}_2^{(1)} + 2g_2^{(3)}\tilde{g}_2^{(3)} + 2\tilde{g}_2^{(3)}\tilde{g}_2^{(3)} + g_4^{(3)}\tilde{g}_4^{(3)} + 2\tilde{g}_4^{(3)}\tilde{g}_4^{(3)} - g_1^{(3)}\tilde{g}_2^{(3)}\right) \quad (35)$$

$$\frac{\partial \tilde{g}_4^{(3)}}{\partial l} = -\frac{1}{\pi v_F}\left(2g_4^{(1)}\tilde{g}_4^{(3)} + g_4^{(3)}\tilde{g}_4^{(1)} + 4\tilde{g}_4^{(1)}\tilde{g}_4^{(3)} + 2g_2^{(1)}\tilde{g}_2^{(3)} + 2g_2^{(3)}\tilde{g}_2^{(1)} + 4\tilde{g}_2^{(1)}\tilde{g}_2^{(3)} - g_4^{(2)}\tilde{g}_4^{(3)} - \tilde{g}_4^{(2)}\tilde{g}_4^{(3)} - g_1^{(2)}\tilde{g}_2^{(3)} - g_1^{(3)}\tilde{g}_2^{(1)}\right) \quad (36)$$

$$\frac{\partial \tilde{g}_4^{(2)}}{\partial l} = -\frac{1}{2\pi v_F}\left(\tilde{g}_4^{(1)}\tilde{g}_4^{(1)} - \tilde{g}_4^{(3)}\tilde{g}_4^{(3)}\right) \quad (37)$$

$$\frac{\partial \tilde{g}_2^{(2)}}{\partial l} = -\frac{1}{2\pi v_F}\left(\tilde{g}_2^{(1)}\tilde{g}_2^{(1)} - \tilde{g}_2^{(3)}\tilde{g}_2^{(3)}\right). \quad (38)$$

Following the flow of the scaling equations, the backscattering and Umklapp interactions are progressively enhanced as the theory is scaled down to low energies.

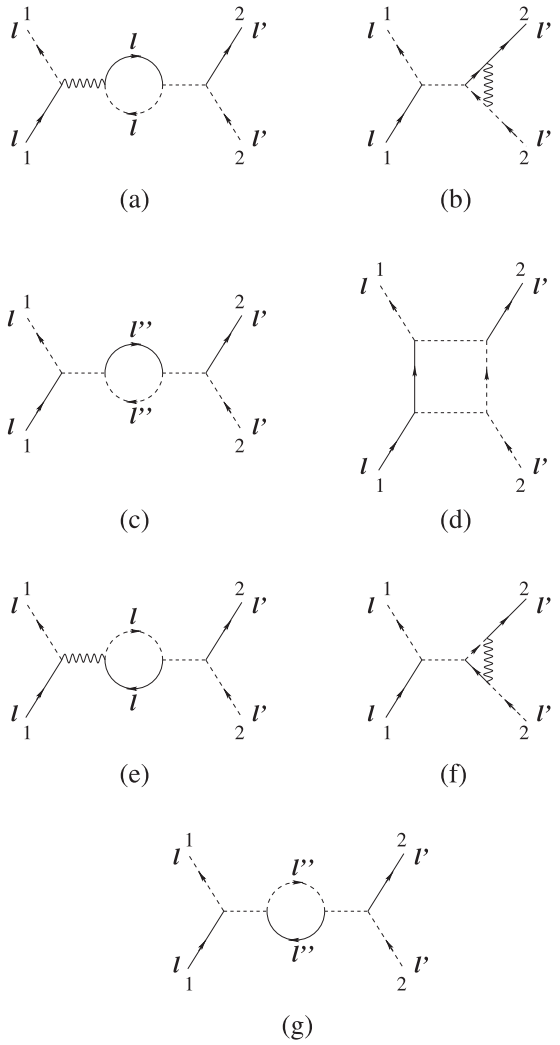

Fig. 9. Second-order diagrams with logarithmic dependence on the frequency renormalizing the intertube $\tilde{g}_2^{(1)}$ interaction. The wavy lines stand for intratube interactions and the dashed lines (without arrow) for interactions between nearest-neighbor nanotubes $\mathbf{l}, \mathbf{l}'$ in a 3D array. The rest of the lines keep the same meaning as in Figure 7.

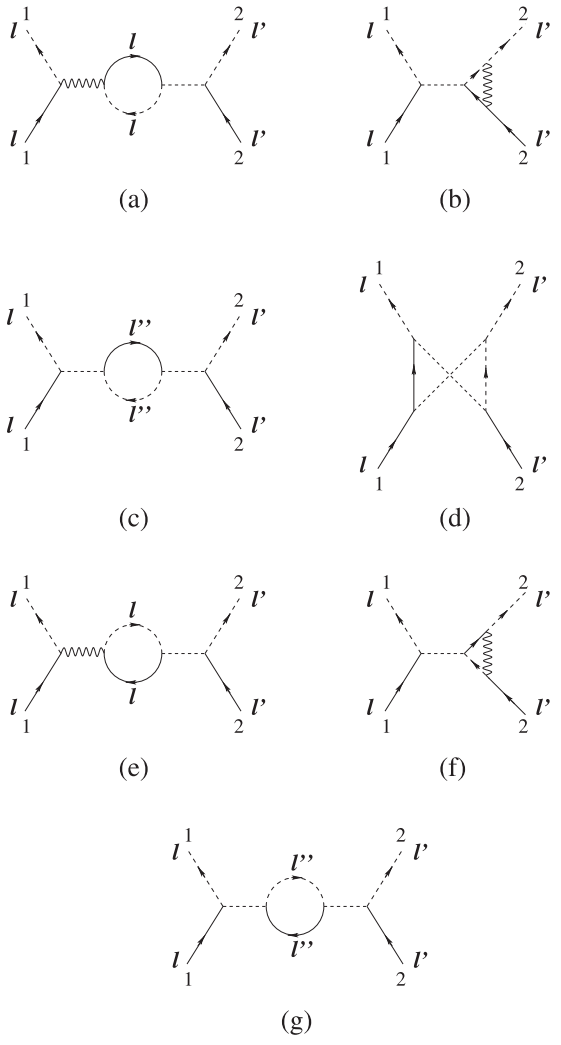

Fig. 10. Second-order diagrams with logarithmic dependence on the frequency renormalizing the intertube $\tilde{g}_2^{(3)}$ interaction. The wavy lines stand for intratube interactions and the dashed lines (without arrow) for interactions between nearest-neighbor nanotubes $\mathbf{l}, \mathbf{l}'$ in a 3D array.

At the initial stage of the renormalization, the values of the couplings are dictated by the Coulomb interaction and, in the case of intratube couplings, also by the effective interaction mediated by phonon-exchange. Regarding the Coulomb interaction, its contribution to forward-scattering couplings is given by the RPA calculation exposed above. Thus we have $g_4^{(4)} = g_2^{(4)} = g_2^{(2)} = g_4^{(2)} = V_{\mathbf{l},\mathbf{l}}^{(r)}(k=0)/v_F$, following the trend shown in Figure 5, while $\tilde{g}_2^{(2)} = \tilde{g}_4^{(2)} = V_{\mathbf{l},\mathbf{l}'}^{(r)}(k=0)/v_F$, with the potential for nearest-neighbor $\mathbf{l}, \mathbf{l}'$ represented in Figure 6. For the chirality-breaking processes, the different symmetry of ingoing and outgoing electron modes implies also a significant reduction of the Coulomb potential, as evaluated in reference [7]. The result is that, for the armchair (3, 3) nanotubes, there is a repulsive component in the backscattering and Umklapp interactions at small momentum-transfer whose strength can be estimated as $\approx 0.23\ v_F/\kappa$. This applies to the couplings $g_2^{(1)}, g_2^{(3)}, g_4^{(1)}$ and $g_4^{(3)}$, as well as to the corresponding intertube couplings at small momentum-transfer. For the intratube couplings with the large momentum-transfer $2k_F$, the contribution by the Coulomb interaction can be obtained from the Fourier transform of the potential (1). The strength estimated in this way turns out to be $\approx 0.06 v_F/\kappa$.

Dealing now with the contribution from the effective phonon-mediated interaction, we note that the situation is reversed, and that the backscattering and Umklapp couplings at vanishing momentum-transfer get a smaller component than the couplings for momentum-transfer around $2k_F$. Previous estimates had already found that the ratio between these two different strengths is approximately 1/3 [28]. More recent calculations of the phonon spectrum by means of density functional theory have

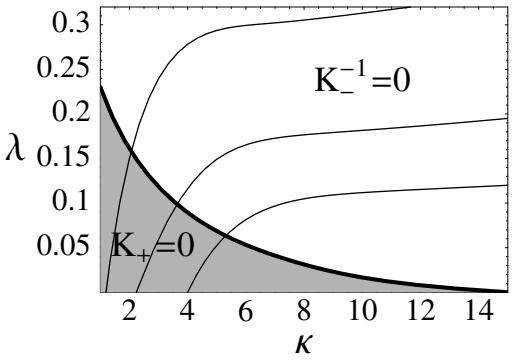

Fig. 11. Phase diagram showing the different low-energy instabilities in the array of (3, 3) nanotubes, depending on the dielectric constant κ and the effective coupling λ of the phonon-mediated interaction. The three thin curves correspond to contour lines of constant critical scale $\omega_c = E_c \exp(-l_c)$, with $l_c = 4, 6, 8$ from top to bottom.

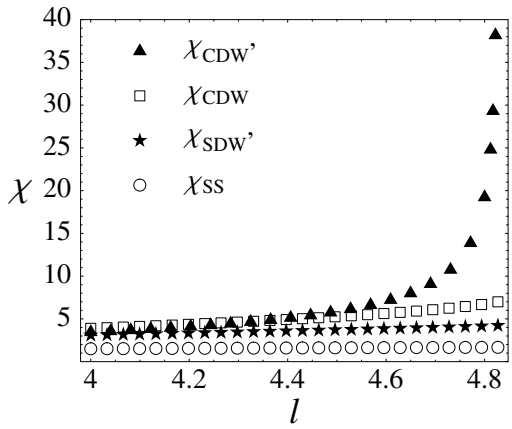

Fig. 12. Plot of different response functions at $\kappa = 2$ and $\lambda = 0.1$.

led to a similar proportion [15]. More precisely, it has been found that the contributions of all the phonons with momentum-transfer $2k_F$ add to an effective coupling $\lambda \approx 0.1$, while the contributions of the phonons near the zone center give an effective coupling $\approx\lambda/3$. These more accurate estimates are about three times smaller than those quoted in reference [28]. Anyhow, we will consider the phase diagram of the (3, 3) nanotubes by spanning a suitable range in the scale λ of the two effective couplings, covering the values between the different estimates in references [15] and [28].

In order to determine the electronic instabilities that may appear at low energies, we have solved the set of scaling equations (24–38), taking initial values for the couplings according to the above discussion. The couplings approach in general a regime where they grow large as $l \to \infty$. Regarding the forward-scattering interactions, $g_4^{(2)}$ becomes increasingly repulsive, leading to a singularity characterized by either the vanishing of K_+ or the divergence of K_-, depending on the region of the phase diagram. The scaling of the interactions stops at the low-energy scale $\omega_c \equiv E_c e^{-lc}$ corresponding to the point l_c where the singularity is reached. This has actually the character of a critical point, since it gives rise to the opening of a branch cut and nonanalytic behavior in the corresponding Luttinger liquid parameter K_+ or K_- [29]. We have plotted in Figure 11 the phase diagram of the (3, 3) nanotubes showing the two different regions of singular behavior, as a function of the dielectric constant κ and the effective coupling λ of the phonon-mediated e–e interaction.

In general, the enhancement of backscattering and Umklapp interactions upon scaling may lead to a large growth of electron correlations, pointing at the tendency towards long-range order in the electron system. We have analyzed this possibility through the computation of different response functions

$$\chi(k,\omega) = -i \int_{-\infty}^{+\infty} dt \int_0^L dx e^{i\omega t} e^{ikx} \langle TO(x,t) O(0,0)^\dagger \rangle \tag{39}$$

where the pair field O characterizes a particular type of ordering. In the system under consideration, the most important correlation functions are found to be given by the following (Fourier transformed) fields:

$$O_{DW,\mu}(k \approx 2k_F) = \frac{1}{2\sqrt{L}} \sum_{p,\alpha,\beta} \Big[\Psi^\dagger_{R1\alpha}(p-k) \sigma_\mu^{\alpha,\beta} \Psi_{L2\beta}(p) + \Psi^\dagger_{L1\alpha}(p-k) \sigma_\mu^{\alpha,\beta} \Psi_{R2\beta}(p) \Big],$$

$$O_{DW',\mu}(k \approx 0) = \frac{1}{2\sqrt{L}} \sum_{p,\alpha,\beta} \Big[\Psi^\dagger_{R1\alpha}(p-k) \sigma_\mu^{\alpha,\beta} \Psi_{L1\beta}(p) + \Psi^\dagger_{R2\alpha}(p-k) \sigma_\mu^{\alpha,\beta} \Psi_{L2\beta}(p) \Big],$$

$$O_{SC,\mu}(k \approx 0) = \frac{1}{2\sqrt{L}} \sum_{p,\alpha,\beta} \alpha \left[\Psi_{R1\alpha}(-p+k) \sigma_\mu^{-\alpha,\beta} \Psi_{L2\beta}(p) + \Psi_{R2\alpha}(-p+k) \sigma_\mu^{-\alpha,\beta} \Psi_{L1\beta}(p) \right],$$

where, for density wave (DW) operators, $\mu = 0$ corresponds to a charge-density wave (CDW) and $\mu = 1, 2, 3$ to a spin-density wave (SDW); while, for superconducting (SC) operators, $\mu = 0$ stands for singlet superconductivity and $\mu = 1, 2, 3$ for triplet superconductivity ($\sigma_\mu^{\alpha,\beta}$ are the Pauli matrices, with $\sigma_0^{\alpha,\beta} = \mathbf{1}_{2\times 2}$).

The derivatives with respect to the frequency of the response functions obey actually scaling equations [24], whose solution allows to compare the relative growth of the different electron correlations. By looking at the low-energy scaling, we have checked however that none of the response functions shows a very large growth, down to the point ω_c where the scaling flow breaks down due to the singularity in the Luttinger liquid parameter. This singular behavior occurs therefore before the appearance of any tendency to long-range order in the electron system. This is illustrated for a typical instance in Figure 12,

where it can be observed that only the CDW correlations with vanishing momentum show a significant growth as the critical point is approached.

We remark that the instabilities that we find in the (3, 3) nanotubes are in wide contrast with respect to those in armchair nanotubes of typical diameter. This can be explained as there are a number of couplings that have a relevant dependence on nanotube diameter. In particular, the Coulomb contribution to backscattering and Umklapp couplings are inversely proportional to the nanotube radius. This also applies to the contributions from phonon-exchange to the same channels, as the electron-phonon couplings are inversely proportional to the square root of the linear mass density. The competition between the Coulomb and the phonon-mediated interaction also takes place in the thicker nanotubes, but the balance leads to a weaker net effective interaction in the mentioned channels. As long as only the backscattering and Umklapp interactions tend to destabilize the Luttinger liquid regime, the instabilities found for instance in the (10, 10) nanotubes turn out to be in general at much lower energy scales than in the (3, 3) nanotubes [29].

Moving to nanotubes of typical thickness, there is also a change in the character of the low-temperature phases, since now the response functions are sensitive to the fact that the scaling extends down to much lower energy scales. In nanotubes of typical diameter, the CDW and SC correlations have a substantial growth at scales which may be more than 3 orders of magnitude below the cutoff E_c. In experimental setups where there is a large number of conducting channels (nanotube ropes, multi-walled nanotubes), the superconductivity turns out to be a weak-coupling effect, driven by a sufficiently large growth of the intertube Cooper-pair tunneling at low energies. In contrast with this picture, the phases characterized by $K_+ = 0$ and $K_-^{-1} = 0$ are found in our analysis as the system enters into the strong-coupling regime, when the ratio of some of the forward-scattering couplings to the Fermi velocity becomes of order 1. This coincides with previous observations that the enhancement of the effective attraction in the small-diameter nanotubes should lead to strong-coupling phases arising from the breakdown of the Luttinger liquid [30], but without implying the transition to a superconducting state.

The physical meaning of the two different phases shown in Figure 11 can be clarified by recalling that K_+ and K_- give the strength of the uniform density correlations. If we define uniform density operators by

$$\rho_\pm(x) = \rho_{L\pm}(x) + \rho_{R\pm}(x) \tag{40}$$

we obtain readily from equations (13) and (14) that

$$\langle \rho_\pm(x)\rho_\pm(0)\rangle \approx \frac{K_\pm}{\pi^2}\frac{1}{x^2}. \tag{41}$$

Thus, the phase given by the divergence of K_- is approached through a regime where the uniform density correlations in the — sector become increasingly large. This signals the tendency of the system to form clusters with a mismatch of charge between the bonding and the antibonding subbands. This effect is a particular realization of the so-called phase separation, in which the appearance of spatial inhomogeneities leads to a breakdown of the description of the system in terms of microscopically averaged variables. The singularity found in K_- is nothing but a reflection of such a breakdown, manifested also in the consequent divergence of the compressibility κ_- obtained from equation (15).

On the other hand, the vanishing of K_+ implies the suppression of the uniform density correlations in the +sector, corresponding to the total charge. This effect does not describe however the transition to an insulating regime, since the system does not become incompressible in the new phase. We recall that the approach to the critical point is driven by the growth of the coupling $g_4^{(2)}$, which leads ultimately to the vanishing of the product u_+K_+ in equation (11). However, the ratio u_+/K_+ in equation (12) remains finite anyhow, implying a nonzero value of the compressibility as given by equation (15). The genuine feature of the phase with $K_+ = 0$ corresponds actually to the vanishing of the renormalized velocity u_+, which has the physical implications discussed below in connection with the phenomenology reported in reference [14].

4 Discussion

The (3, 3) carbon nanotubes may fall therefore into two different low-temperature phases, whose physical properties are dictated by the vanishing of K_+ and the divergence of K_- respectively. We remind in particular that, for the experimental setup of reference [14], a reasonable choice of the parameters is $\kappa \sim 2 \div 4$ and $\lambda \sim 0.1$, corresponding to the $K_+ = 0$ phase. In this case the temperature of transition to the new phase results strongly dependent on the dielectric constant of the environment, ranging from $T_c \sim 10^{-1}$ K (at $\kappa \approx 2$) to $T_c \sim 10$ K (at $\kappa \approx 4$).

The behavior of the response functions follows in general the trend shown in Figure 12 and, while the density-wave correlations tend to grow by approaching the critical value l_c, the superconducting correlations remain small anyhow. This finding seems to rule out the possibility of having superconducting correlations in the (3, 3) nanotubes, at least under the physical conditions considered in the present paper. We coincide in this respect with the conclusions reached in previous analyses by means of other computational methods [15,16]. We have found however that the appearance of a CDW instability is precluded by the breakdown of the Luttinger liquid behavior, which cuts off the growth of the different correlations.

Our results confront the claim that the experimental signatures reported in reference [14] should provide evidence for a superconducting transition in the small-diameter nanotubes. This interpretation has been also challenged by studies of the electron correlations in the (5, 0) nanotubes [15,31]. We have shown that, even considering the large screening effects from the arrays of

nanotubes in the experimental samples, the effective e–e attraction arising from the exchange of phonons is not large enough to support the appearance of superconducting correlations in the (3, 3) nanotubes. If the Coulomb interaction is further screened by a suitable variation of the dielectric constant of the medium, the system is driven then into the phase characterized by the divergence of K_- and the related compressibility κ_-, as shown in Figure 11. This has the same character that the instability given by the Wentzel-Bardeen singularity, where the divergent compressibility is the signal of the spatial separation of the system into regions with different electron density [30,32].

Anyhow, the experimental conditions of the samples described in reference [14] seem to place the system in the region of the phase diagram characterized by the vanishing of K_+. As explained above, the critical point at $K_+ = 0$ does not describe a conventional metal-insulator transition, as long as the compressibility κ_+ remains always nonvanishing. However, the decay of K_+ leads to the vanishing of the differential conductivity, which is directly related to the tunneling density of states $n(\varepsilon)$. The strong suppression of this quantity is a manifestation of the absence of electron quasiparticles in the system. Within the Luttinger liquid framework, the tunneling density of states follows the low-energy behavior

$$n(\varepsilon) \sim \varepsilon^{(K_+ + 1/K_+ + K_- + 1/K_- - 4)/8}. \qquad (42)$$

The approach to the critical point at $K_+ = 0$ is controlled in our model by the logarithm l of the low-energy scale, which must be put in correspondence with the temperature variable in the experiments. What we observe from equation (42) is that the density of states follows a power-law behavior, with an increasingly large exponent as the point of the transition is approached. This kind of depletion of the density of states is consistent with the appearance of the pseudogap observed in the $I-V$ characteristics reported in reference [14]. A quantitative comparison with the experimental data is precluded by the fact that the measure of the voltage characterizing the pseudogap comes from the sum of multiple voltage drops, as the nanotubes are cut along the longitudinal direction into a very large number of segments. It is anyhow remarkable that the pseudogap develops through an evolution of the $I - V$ curves which is qualitatively similar to that of a power-law behavior with divergent exponent for decreasing temperature.

As observed above, the distinctive feature of the phase with $K_+ = 0$ is actually the vanishing of the product u_+K_+. This quantity appears in the Hamiltonian (10), in front of the square of the momentum $\Pi_+(x)$. This operator corresponds to the total current in the electron system, so that the quantity u_+K_+ plays therefore the role of a current velocity [33]. Thus, the essence of the phase with $K_+ = 0$ is to be found, on physical grounds, in the appearance of very soft modes in the sector of current excitations. This has important implications regarding the magnetic properties, since the vector potential couples naturally to the total current. The vanishing of the current velocity u_+K_+ leads to the divergence of the current-current response function, which is proportional to $1/u_+K_+$ in the static limit [33]. As analyzed in reference [34], this is in agreement with the behavior of the magnetic susceptibility observed experimentally, which has a divergence at low temperature concomitant with the development of the pseudogap. We conclude therefore that the phenomenology derived from the $K_+ = 0$ phase of the (3, 3) carbon nanotubes seems to be consistent, at least qualitatively, with the main experimental signatures reported in reference [14]. Further experimental work would be needed to clarify the existence of such a critical point in the (3, 3) nanotubes, its physical properties, and its stability under changes of relevant experimental conditions.

The financial support of the Ministerio de Educación y Ciencia (Spain) through grants BFM2003-05317 and FIS2005-05478-C02-02 is gratefully acknowledged. E.P. was also supported by INFN grant 10068.

References

1. J.W. Mintmire, B.I. Dunlap, C.T. White, Phys. Rev. Lett. **68**, 631 (1992)
2. R. Saito, M. Fujita, G. Dresselhaus, M.S. Dresselhaus, Appl. Phys. Lett. **60**, 2204 (1992); N. Hamada, S. Sawada, A. Oshiyama, Phys. Rev. Lett. **68**, 1579 (1992)
3. A.Yu. Kasumov, R. Deblock, M. Kociak, B. Reulet, H. Bouchiat, I.I. Khodos, Yu.B. Gorbatov, V.T. Volkov, C. Journet, M. Burghard, Science **284**, 1508 (1999)
4. M. Bockrath, D.H. Cobden, J. Lu, A.G. Rinzler, R.E. Smalley, L. Balents, P.L. McEuen, Nature **397**, 598 (1999)
5. Z. Yao, H.W.Ch. Postma, L. Balents, C. Dekker, Nature **402**, 273 (1999)
6. L. Balents, M.P.A. Fisher, Phys. Rev. B **55**, R11973 (1997)
7. R. Egger, A.O. Gogolin, Phys. Rev. Lett. **79**, 5082 (1997); R. Egger, A.O. Gogolin, Eur. Phys. J. B **3**, 281 (1998)
8. C. Kane, L. Balents, M.P.A. Fisher, Phys. Rev. Lett. **79**, 5086 (1997)
9. H. Yoshioka, A.A. Odintsov, Phys. Rev. Lett. **82**, 374 (1999); Phys. Rev. B **59**, R10457 (1999)
10. A.A. Nersesyan, A.M. Tsvelik, Phys. Rev. B **68**, 235419 (2003)
11. M. Kociak, A.Yu. Kasumov, S. Guéron, B. Reulet, I.I. Khodos, Yu.B. Gorbatov, V.T. Volkov, L. Vaccarini, H. Bouchiat, Phys. Rev. Lett. **86**, 2416 (2001)
12. A. Kasumov, M. Kociak, M. Ferrier, R. Deblock, S. Guéron, B. Reulet, I. Khodos, O. Stéphan, H. Bouchiat, Phys. Rev. B **68**, 214521 (2003)
13. M.T. Figge, M. Mostovoy, J. Knoester, Phys. Rev. B **65**, 125416 (2002)
14. Z.K. Tang, L. Zhang, N. Wang, X.X. Zhang, G.H. Wen, G.D. Li, J.N. Wang, C.T. Chan, P. Sheng, Science **292**, 2462 (2001)
15. D. Connétable, G.-M. Rignanese, J.-C. Charlier, X. Blase, Phys. Rev. Lett. **94**, 015503 (2005)
16. K.-P. Bohnen, R. Heid, H.J. Liu, C.T. Chan, Phys. Rev. Lett. **93**, 245501 (2004)
17. R. Barnett, E. Demler, E. Kaxiras, Phys. Rev. B **71**, 035429 (2005)
18. J. González, Phys. Rev. Lett. **87**, 136401 (2001)

19. J. González, Phys. Rev. Lett. **88**, 076403 (2002); J. González, Phys. Rev. B **67**, 014528 (2003)
20. D.W. Wang, A.J. Millis, S. Das Sarma, Phys. Rev. B **64**, 193307 (2001)
21. H.J. Liu, C.T. Chan, Phys. Rev. B **66**, 115416 (2002)
22. Yu.A. Krotov, D.-H. Lee, S.G. Louie, Phys. Rev. Lett. **78**, 4245 (1997)
23. V.J. Emery, in *Highly Conducting One-Dimensional Solids*, edited by J.T. Devreese, R.P. Evrard, V.E. Van Doren (Plenum, New York, 1979)
24. J. Sólyom, Adv. Phys. **28**, 201 (1979)
25. A.O. Gogolin, A.A. Nersesyan, A.M. Tsvelik, *Bosonization and Strongly Correlated Systems* (Cambridge Univ. Press, Cambridge, 1998)
26. H.J. Schulz, in *Correlated Electron Systems*, edited by V.J. Emery, Vol. 9 (World Scientific, Singapore, 1993)
27. P. Hawrylak, G. Eliasson, J.J. Quinn, Phys. Rev. B **37**, 10187 (1988)
28. A. Sédéki, L.G. Caron, C. Bourbonnais, Phys. Rev. B **65**, 140515 (2002)
29. J.V. Alvarez, J. González, Phys. Rev. Lett. **91**, 076401 (2003)
30. A. De Martino, R. Egger, Phys. Rev. B **67**, 235418 (2003)
31. J. González, E. Perfetto, Phys. Rev. B **72**, 205406 (2005)
32. D. Loss, T. Martin, Phys. Rev. B **50**, 12160 (1994)
33. J. Voit, Rep. Prog. Phys. **58**, 977 (1995)
34. J. González, Phys. Rev. B **72**, 073403 (2005)